



ELSEVIER

Contents lists available at ScienceDirect

# Medical Image Analysis

journal homepage: [www.elsevier.com/locate/media](http://www.elsevier.com/locate/media)

## Challenge Report

# A bi-atrial statistical shape model for large-scale in silico studies of human atria: Model development and application to ECG simulations

Claudia Nagel\*, Steffen Schuler, Olaf Dössel, Axel Loewe

*Institute of Biomedical Engineering (IBT), Karlsruhe Institute of Technology (KIT), Kaiserstr. 12, Karlsruhe 76131, Germany*

## ARTICLE INFO

### Article history:

Received 11 December 2020

Revised 29 June 2021

Accepted 4 August 2021

Available online 10 August 2021

### MSC:

51E99

60G15

62H25

### Keywords:

Statistical shape modeling

Bi-atrial shape model

Electrophysiological simulation

12-Lead ECG

P waves

## ABSTRACT

Large-scale electrophysiological simulations to obtain electrocardiograms (ECG) carry the potential to produce extensive datasets for training of machine learning classifiers to, e.g., discriminate between different cardiac pathologies. The adoption of simulations for these purposes is limited due to a lack of ready-to-use models covering atrial anatomical variability.

We built a bi-atrial statistical shape model (SSM) of the endocardial wall based on 47 segmented human CT and MRI datasets using Gaussian process morphable models. Generalization, specificity, and compactness metrics were evaluated. The SSM was applied to simulate atrial ECGs in 100 random volumetric instances.

The first eigenmode of our SSM reflects a change of the total volume of both atria, the second the asymmetry between left vs. right atrial volume, the third a change in the prominence of the atrial appendages. The SSM is capable of generalizing well to unseen geometries and 95% of the total shape variance is covered by its first 24 eigenvectors. The P waves in the 12-lead ECG of 100 random instances showed a duration of  $109.7 \pm 12.2$  ms in accordance with large cohort studies. The novel bi-atrial SSM itself as well as 100 exemplary instances with rule-based augmentation of atrial wall thickness, fiber orientation, inter-atrial bridges and tags for anatomical structures have been made publicly available.

This novel, openly available bi-atrial SSM can in future be employed to generate large sets of realistic atrial geometries as a basis for in silico big data approaches.

© 2021 The Authors. Published by Elsevier B.V.

This is an open access article under the CC BY license (<http://creativecommons.org/licenses/by/4.0/>)

## 1. Introduction

A wide range of machine learning approaches have already been proposed for classifying cardiovascular pathologies based on the 12-lead electrocardiogram (ECG) (Hannun et al., 2019; Perez Al-day et al., 2020; Strodthoff et al., 2020). Since the ECG is a cost-effective, non-invasive and commonly available tool in clinical practice, it is particularly desirable to identify and diagnose cardiac pathologies only based on the ECG and without the need of further expensive imaging techniques or invasive procedures. However, the training of such classifiers requires a large, balanced, and reliably labeled dataset. Oftentimes, not all of these prerequisites are met when using clinically recorded data. Additionally, expert annotations are commonly relied upon to generate the ground truth labels describing the underlying pathologies for clinical datasets coming along with inter- and intra-observer variability

significantly affecting the reliability of the ground truth labels (Hannun et al., 2019).

These limitations call for simulated synthetic ECG as a source for large, representative and well controlled datasets. These datasets can be used to directly deduce diagnostic criteria visually (Andlauer et al., 2018) or to train machine learning classifiers to discriminate between different cardiac diseases and healthy individuals (Andlauer et al., 2018). The advantage of using simulated over clinical data lies not only in the precisely known ground truth of the underlying pathology that was defined for the simulation, but also in the possibility to generate a virtually infinite amount of signals for each pathology class.

Nevertheless, atrial, ventricular and thoracic geometrical models are needed for conducting electrophysiological simulations to obtain the 12-lead ECG. In this regard, statistical shape models (SSM) allow to compile a wide range of realistic geometries that represent the variability observed in the cohort used to build the SSM. While SSMs of the human ventricles (Bai et al., 2015) and torsos (Pishchulin et al., 2017) exist and are publicly available, an open shape model of both atria covering all relevant anatomical struc-

\* Corresponding author..

E-mail addresses: [publications@ibt.kit.edu](mailto:publications@ibt.kit.edu), [claudia.nagel@kit.edu](mailto:claudia.nagel@kit.edu) (C. Nagel).

tures for EP simulations (atrial body, appendages, PVs) is still lacking to the best of our knowledge.

Different statistical atlases of the human whole heart anatomy (Ecabert et al., 2008; Hoogendoorn et al., 2013; Lötjönen et al., 2004; Ordas et al., 2007; Unberath et al., 2015; Zhuang et al., 2010) have been constructed for segmentation of magnetic resonance (MR) or computed tomography (CT) images by means of active shape modeling approaches. However, those models are usually built based on a small number of sample segmentations or were not made publicly available. Furthermore, different SSMs of only the left atrium (LA) have been presented in various studies either for the purpose of simulations (Corrado et al., 2020) or for characterizing changes in shape of the LA (Bieging et al., 2018; Cates et al., 2014; Depa et al., 2010; Varela et al., 2017) in patients with atrial fibrillation. These LA models are built based on a solid number of instances, but lack the right atrium (RA) and often also the left atrial appendage (LAA). However, these anatomical structures are not only indispensable for the use case of ECG simulations. They are also of particular importance when investigating the mechanisms of typical atrial flutter in the RA or bi-atrial flutter and fibrillation. Additionally, the LAA is highly relevant for studies examining blood clot formation causing stroke (Masci et al., 2019), LAA occlusion as potential therapy (Aguado et al., 2019) and the role of the LAA in the onset and maintenance of atrial fibrillation (Nishimura et al., 2019). Due to the lack of ready-to-use models of the atria, a bi-atrial SSM would cater the need of generating geometrical atrial models representing inter-subject anatomical variability. These could be employed to gain a comprehensive understanding of the underlying mechanisms of the onset and perpetuation of re-entrant activity during atrial flutter and fibrillation not only in personalized computer models but also in a large patient cohort. Thus, including the shape of the RA in the model as well as making the bi-atrial SSM available to the community, enables large-scale simulation of atrial signals. Although the focus of this paper is the application of the SSM for ECG simulations, its field of application is not limited to this particular use case. The bi-atrial model can also be exploited for other *in silico* approaches like continuum-mechanics and fluid simulations. Furthermore, active shape modeling approaches using the novel bi-atrial SSM could facilitate automated segmentation of the atria from CT or MRI datasets.

In this work, we built an SSM of both atria from manual segmentations of 47 MR and CT scans. Furthermore, we propose a workflow to generate a volumetric atrial model based on instances of the SSM. A major added value of our study for the community is the provision of the bi-atrial SSM under the creative commons license CC-BY 4.0 together with 100 exemplary volumetric models derived from it including fiber orientation, inter-atrial bridges, material tags and solutions to Laplace's equation (Nagel et al., 2021).

## 2. Material and methods

The geometric representation as well as the variation in shape among a set of individual three dimensional objects can be described by SSMs. Point distribution models (Cootes et al., 1995) are the most common subclass of SSMs and require a vectorized point-based representation  $\mathbf{s}_n$  of any individual geometry  $\Gamma_n$  comprising  $M$  consistently sampled surface points  $[\mathbf{x}_n, \mathbf{y}_n, \mathbf{z}_n]^T$ :

$$\mathbf{s}_n = [x_{n,1}, y_{n,1}, z_{n,1}, \dots, x_{n,M}, y_{n,M}, z_{n,M}]^T. \quad (1)$$

Assuming that the spatial variations of the surface points follow a multivariate normal distribution, a compact representation of the mean and covariance matrix describing the shape variations can be obtained by applying a principal component analysis (PCA) to the observations  $\mathbf{s}$ . In this way, all  $N$  individual shapes  $\Gamma$  can be

represented by a linear combination of  $N - 1$  basis functions  $\mathbf{v}$ :

$$\mathbf{s}_n = \bar{\mathbf{s}} + \sum_{k=1}^{N-1} r_{n,k} \cdot \sqrt{\sigma_k^2} \cdot \mathbf{v}_k \quad (2)$$

with  $\bar{\mathbf{s}}$  being the mean shape vector as well as  $\sigma$  and  $\mathbf{v}$  representing the eigenvalues and eigenvectors of the covariance matrix, respectively.  $r_{n,k}$  represent the weighting coefficients for the individual eigenvectors. To obtain this parametric representation of the shape variations from clinical MRI or CT data, a number of pre-processing steps have to be performed: i) segmenting the images, preferably in a (semi-)automatic manner, ii) rigidly aligning the resulting shapes in space, iii) establishing a dense correspondence between the individual shapes to obtain the shape vectors  $\mathbf{s}^c$  that were then subject to PCA.

### 2.1. Dataset

Three independent multi-center, multi-vendor databases (Karim et al., 2013; 2018; Tobon-Gomez et al., 2015) were used to build the SSM. Their properties are summarized in Table 1. The images originate either from healthy subjects or from patients suffering from atrial fibrillation. Since all of the challenges focused on the segmentation of the LA, 23 of the originally available images had to be excluded due to an incomplete capture of the inferior right atrial body or an inadequate signal to noise ratio. Since we relied on a PCA description for representing the atrial shape variability with which only continuous changes of vertex locations are representable, only subjects with 4 pulmonary veins (PVs) were considered. The number of PVs attached to a subject's atrium is discrete and the absence or the presence of an additional PV is not characterized by a continuous transition which is why only data samples of patients with 4 PVs were included in this study. According to Marom et al. (2004), this PV configuration is representative for the majority of the population with 71% and 86% of all subjects in their study exhibiting two ostia on the right and left side of the LA body, respectively.

### 2.2. Segmentation

In order to obtain the individual instances of both atria, a semi-automatic segmentation of the blood pool representing the endocardial surface of the left and the right atrium from MR and CT images was performed using CemrgApp (Razeghi et al., 2020). 2D region growing in several selected slices as well as 3D interpolation were applied to each image stack. To reduce the impact of noise or image artefacts on the segmentation outcome, details were manually corrected.

Fig. 1 shows examples of incorrect segmentation results due to insufficient region growing performance (left column) and 3D interpolation (middle column) that made a manual correction indispensable. Automated segmentation with region growing especially failed in 2D planes where both, the LA and the left ventricle are visible, because the mitral valve shows the same image intensity as the LA and the left ventricle. Therefore, a cutting plane between atrium and ventricle was inserted manually. The drawbacks of 3D interpolation are particularly affecting the areas around the PVs where the interpolated surface tends to close small gaps between the PVs and the atrial body. For 20 images in dataset 2, a segmentation of the LA was provided. However, the LAA was truncated in close proximity to the left atrial body (Tobon-Gomez et al., 2015) in these segmentations. Since we aimed at incorporating the variability of the LAA shape in our model, the LA segmentations of dataset 2 were adapted to include the full volume of the LAA as shown in Fig. 1 (right column). The resulting segmentations were exported as triangular meshes.

**Table 1**  
Summary of datasets used to generate the statistical shape model.

Dataset	Source	Number of subjects	Voxel resolution
1	Left atrium segmentation challenge (Tobon-Gomez et al., 2015)	30 MRI	1.25 x 1.25 x 2.7 mm
2	Left atrium fibrosis and scar segmentation challenge (Karim et al., 2013)	8 MRI	1.25 x 1.25 x 2.5 mm 1.4 x 1.4 x 1.4 mm
3	Left atrial wall thickness challenge (Karim et al., 2018)	9 CT	0.8 x 1 x 0.4 mm

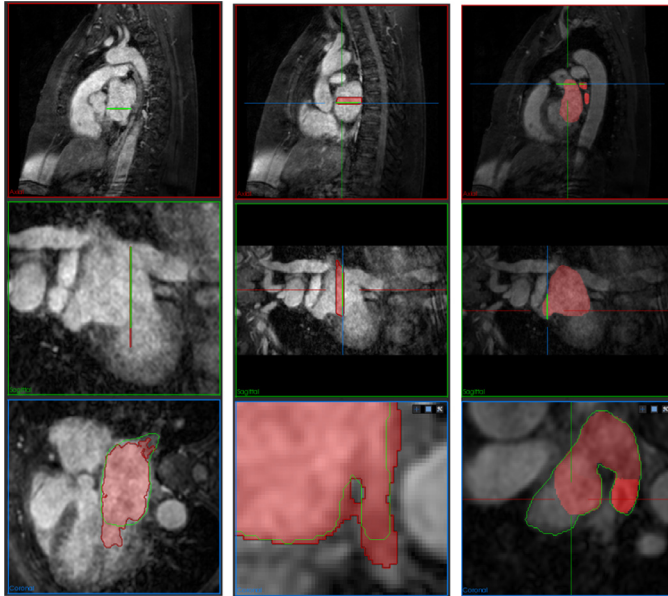


**Fig. 1.** Segmentation inaccuracy due to different automated segmentation methods. The different rows represent the axial, sagittal and the coronal plane, respectively. The images in the left, middle and right column show the segmentation errors due to region growing, 3D interpolation and a partly excluded LAA in the ground truth data colored in red, respectively. The green contours mark the manual corrections tailored to the correction of inaccurately found automated segmentations. (For interpretation of the references to colour in this figure legend, the reader is referred to the web version of this article.)

### 2.3. Rigid alignment

After segmenting the individual instances  $\Gamma_n$  of the atria, the resulting isosurfaces exported from CemrgApp were rigidly aligned in space to avoid a representation of translation and rotation parameters in the eigenmodes of the SSM. This was performed automatically by means of the iterative closest point (ICP) algorithm that provides a solution to the orthogonal Procrustes problem (Chen and Medioni, 1992). Surface-to-surface distances were calculated with the *vtkDistancePolyDataFilter* (Kitware, Clifton Park, New York, USA) between each pair of individual instances  $\Gamma_n$ . The reference template was chosen as the surface holding the lowest mean distance to all other instances. In each iteration  $i$ , candidate correspondences  $[\hat{\mathbf{x}}_n, \hat{\mathbf{y}}_n, \hat{\mathbf{z}}_n]_{R,i}^T$  between a target mesh  $\Gamma_n$  and the reference mesh  $\Gamma_R$  were found by attributing to each node in  $\Gamma_n$  the point with the smallest Euclidean distance in  $\Gamma_R$ . Procrustes analysis was then used to estimate the linear transformation  $\mathbf{T}_i$  – consisting of rotation and translation – which yields the best match of the candidate correspondence points  $[\hat{\mathbf{x}}_n, \hat{\mathbf{y}}_n, \hat{\mathbf{z}}_n]_{R,i}^T$  with the reference points  $[\mathbf{x}_R, \mathbf{y}_R, \mathbf{z}_R]^T$ . After applying the estimated transformation  $\mathbf{T}_i$  to the points in mesh  $\Gamma_n$ :

$$\tilde{\Gamma}_{n,i+1} = \mathbf{T}_i \cdot \tilde{\Gamma}_{n,i}, \quad \text{with } \tilde{\Gamma}_{n,0} = \Gamma_n \quad (3)$$

new candidate correspondences  $[\hat{\mathbf{x}}_n, \hat{\mathbf{y}}_n, \hat{\mathbf{z}}_n]_{R,i+1}^T$  are recursively found between the transformed mesh  $\tilde{\Gamma}_{n,i+1}$  and  $\Gamma_R$  at each iteration  $i$  and used for solving the Procrustes problem. If after several recursive calls of the function, either the maximum number of 150 iterations is exceeded or the convergence criterion is fulfilled, an optimal transformation matrix for the alignment of both shapes  $\Gamma_n$  and  $\Gamma_R$  is found resulting in a set of  $N$  rigidly aligned shapes  $\Gamma^A$ .

### 2.4. Establishment of correspondence

Each aligned individual instance  $n$  comprises  $M_n$  surface points  $[x_{n,1}^A, y_{n,1}^A, z_{n,1}^A, \dots, x_{n,M_n}^A, y_{n,M_n}^A, z_{n,M_n}^A]^T$ . In order to describe the variations in shape of the aligned instances  $\Gamma^A$  by means of a point distribution model, correspondence between the vertex IDs among all individual shapes have to be established. Establishing correspondence requires to retrieve concordant points in all shapes  $\Gamma^A$ , so that the  $N$  aligned shapes are not only represented by the same amount of surface points  $M$  but also that each point  $[x_{n,m}^A, y_{n,m}^A, z_{n,m}^A]$  with a specific ID  $m$  represents the same anatomical landmark in any arbitrary shape  $n$ . For this purpose, we used Gaussian process morphable models (GPMM) (Luthi et al., 2018) and ScalismoLab (Bouabene et al., 2020) to subject a reference shape  $\Gamma_R^A$  to a generic deformation in such a way that the deformed shape  $\tilde{\Gamma}_{R,n}^A$  matches the individual aligned shape  $\Gamma_n^A$  in the best possible way. This process then yields a set  $\Gamma^C$  of aligned shapes that are characterized by homologous, corresponding surface points. For this process, we defined three independent generic deformations by Gaussian process (GP) models. Gaussian kernels described the similarity between two distinct points  $\mathbf{x}$  and  $\mathbf{x}'$ :

$$k(\mathbf{x}, \mathbf{x}') = s \cdot \exp\left(-\frac{(\mathbf{x} - \mathbf{x}')^2}{l^2}\right) \quad (4)$$

were approximated by the leading eigenfunctions of their Karhunen-Loève expansion as described in Luthi et al. (2018). They were further employed to fit the orientation of the left and right pulmonary veins (LPV, RPV), the atrial body, as well as the left and the right atrial appendages (LAA, RAA). The separation into three different models (atrial body, appendages, PVs) served two different purposes. On the one hand, we were able to account for the high anatomical variability of the appendages by allowing smaller inter-dependencies spanning between the points located on the appendages. On the other hand, the generic model varying the points located on the PVs was designed such that only the orientation of the PV ostia but not their length was affected. We used built-in functions of Scalismo (Bouabene et al., 2020) to successively fit the three anatomical regions of each aligned observation  $\Gamma_n^A$  with a custom PV model and a generic deformation for the appendages and the atrial body. The optimization problem of fitting the GP model  $\tilde{\Gamma}_{R,n}^A$  to the individual aligned shapes  $\Gamma_n^A$  was solved using the *Registration* built-in class in Scalismo with an L-BFGS optimization minimizing the mean squared error between the vertex coordinates of the deformed model  $\tilde{\Gamma}_{R,n}^A$  and the target shape  $\Gamma_n^A$ . To accurately fit the PVs, a kernel representing the orientation of the four PVs in anterior-posterior direction in its first four eigenvectors was constructed (Fig. 2). This custom kernel was built by

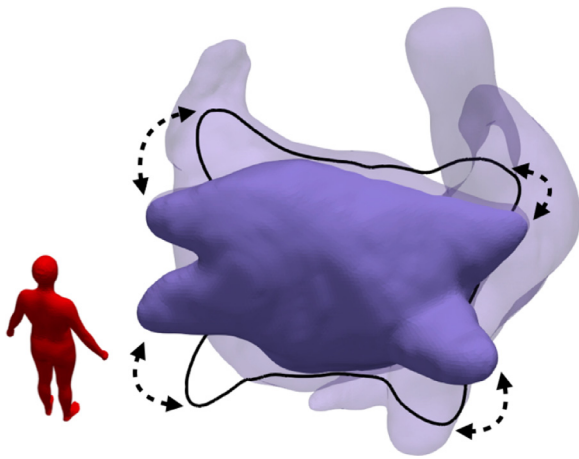


**Fig. 2.** Morphable model for establishing correspondence at the PVs. The arrows indicate the movement of the respective vertices in the model for a variation of the four leading eigenvectors by  $-3\sigma$  and  $+3\sigma$ . The LA body and the RA shape are not affected by this PV model and are visualized in a semi-transparent manner.

manually moving each of the four PVs of the reference shape  $\Gamma_R^A$  in two different directions at a time using Meshmixer (Autodesk, San Rafael, CA, USA). Disabling the mesh refinement option during this process ensured that the resulting eight shapes differed from one another only in their PV orientation and were in correspondence. Therefore, they could directly be applied to construct the custom PV model (Fig. 2). We intentionally did not fit the length of the PVs since this quantity highly depends on the segmentation approach and does therefore not represent a proper observed anatomical variation considering the heterogeneous input data used in this study. A low rank approximation of a GP model was realized using the *LowRankGaussianProcess* class in Scalismo with an empirically chosen variance of  $s_b = 50$ ,  $l_b = 40$  at points representing the general atrial body ( $b$ ) and  $s_a = 20$ ,  $l_a = 20$  at the appendages to account for the higher anatomical variability in the appendage ( $a$ ) regions.

### 2.5. Shape model construction

The vertices at the distal parts of the superior and inferior caval veins, the coronary sinus, the PVs, as well as the mitral valve and the tricuspid valve were discarded from the  $N$  aligned shape vectors in correspondence  $\mathbf{s}^C$  to limit the model creation to atrial components relevant for electrophysiological simulations. Applying a PCA to these cut shape vectors in correspondence  $\mathbf{s}^C$  yields their mean shape  $\bar{\mathbf{s}}$  and  $N - 1$  basis functions  $\mathbf{v}$  along with their respective variances  $\sigma^2$ . In this way, an exact reconstruction of any individual shape instance  $\Gamma_n^C$  is feasible by determining the coefficients  $\mathbf{r}_n$  in Eq. 2 with a standard least squares estimation. Furthermore, additional arbitrary variation shapes  $\Gamma_{var}$  in the span of the  $N - 1$  basis vectors  $\mathbf{v}$  can be derived by varying  $\mathbf{r}$ . Under the assumption that the values of  $\mathbf{r}$  are normally distributed among the observed instances  $\Gamma_n^C$ , keeping  $\mathbf{r}$  in the interval  $[-3, +3]^{N-1}$  yields realistic artificially generated shapes within the empirically observed variability.

### 2.6. Construction of volumetric meshes

The bi-atrial SSM represents the mean shape of the atrial endocardial surface and the variation of all point coordinates in space so that any arbitrary variation mesh  $\Gamma_{var}$  can be derived from it. However, a volumetric model of the atria, including inter-atrial

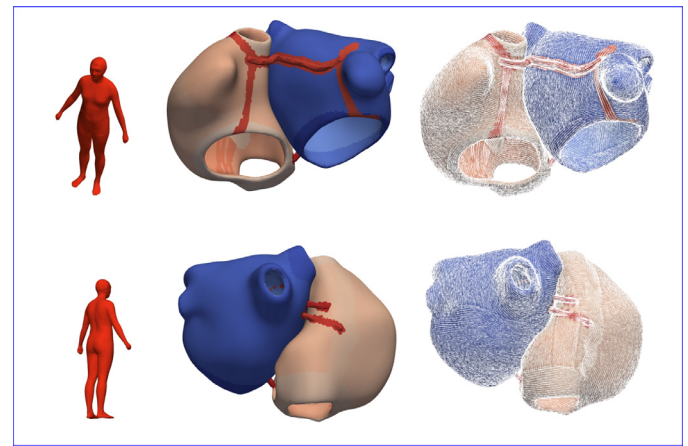


**Fig. 3.** Example of one randomly generated instance with a homogeneous wall thickness from two different views. The models on the left represent the anatomical labels and the inserted inter-atrial bridges. The fiber orientations are visualized on the models in the right column.

bridges, anatomical labels and fiber orientations is required to perform electrophysiological simulations and to obtain realistic body surface P waves. We therefore developed a workflow to fully automatically create a volumetric model based on an arbitrary endocardial surface. Since a segmentation of the epicardial surface from conventional MR images is usually not feasible due to an insufficient spatial resolution and a limited signal to noise ratio, the epicardial surface was augmented in a postprocessing step assuming a homogeneous atrial wall thickness. To approximate the epicardial surface, the endocardial surface of the variation mesh  $\Gamma_{var}$  was dilated by 3 mm (Whitaker et al., 2016) at each point along the normal direction calculated as the mean of the adjacent triangle normals. Both surfaces were merged and intersections and holes between epi- and endocardium were corrected and closed automatically using the iso2mesh toolbox (Tran et al., 2020). The closed surface was afterwards remeshed using Instant Meshes (Jakob et al., 2015) and transformed into a volumetric tetrahedral mesh with an average edge length of 1 mm using Gmsh (Geuzaine and Remacle, 2009). Contact and integrity between left and right atrium were preserved by duplicating the epicardial nodes belonging to the septum in regions where the left and the right epicardial surfaces spatially overlapped. The affected endocardial nodes were subsequently moved in negative direction of the surface normals to ensure a homogeneous wall thickness of 3 mm. The algorithms described by Piersanti et al. (2021) and Wachter et al. (2015) were used to automatically augment the models with Bachmann's bundle, a coronary sinus and an upper and middle posterior inter-atrial connection between the LA and RA as well as myocardial fiber orientation and anatomical labels. The augmented anatomical structures are visualized in Fig. 3. The only manual input required for augmenting the volumetric geometry with the aforementioned structures consists of 4 seed points defining the tips of the appendages and landmarks for the Bachmann's bundle connection. They were defined once on the mean shape and were tracked through the deformations for any arbitrary variation mesh. In this way, it was ensured that the seed points were consistently chosen among all variation meshes.

### 2.7. Parameterization of electrophysiological simulations

100 random instances were derived from the bi-atrial SSM by drawing the eigenvector coefficients  $\mathbf{r}$  of Eq. 2 from a Gaussian distribution in the  $[-3, +3]\sigma$  range. A fast marching (Loewe et al.,

**Table 2**

Conduction velocity (CV) along the transversal fiber direction in mm/s and anisotropy ratios (AR) in different atrial regions.

Atrial Region	$CV_T$ (mm/s)	AR
Right atrium	739	2.11
Left atrium	946	2.11
Inter-atrial connections	1093	3.36
Valve rings	445	2.11
Pectinate muscles	578	3.78
Crista Terminalis	607	3.0
Inferior isthmus	722	1

2019; Sethian, 1996) simulation was carried out for solving the Eikonal equation on these 100 geometries to obtain the spread of electrical activation and derive local electrical activation times (LATs) for each node. This sinus rhythm activation was initiated from a sinus node exit site located at the junction of the superior caval vein and the RAA (Loewe et al., 2016). The atrial wall was separated into seven different anatomical regions: regular right and left atrium, inter-atrial connections, valve rings, pectinate muscles, crista terminalis and inferior isthmus. The conduction velocities along the fiber directions and the anisotropy ratios in the different regions were chosen as reported previously (Loewe et al., 2016) and are given in Table 2.

The transmembrane voltage distribution on the atrial surfaces was obtained by shifting a pre-computed Courtemanche et al. (1998) action potential in time according to the calculated LATs as proposed by (Kahlmann et al., 2017). The ECG forward problem to derive the body surface potentials from the transmembrane distribution on the heart was solved by means of the boundary element method (Stenroos et al., 2007). Considering computational cost, the surface bounding the heart was sampled at a resolution of 3 mm. Laplacian blurring with optimal blurring parameters as described in Schuler et al. (2019) was applied to the source distribution. The mean shape of the human body SSM developed by Pishchulin et al. (2017) served as a reference shape of the torso. The P wave of the 12-lead ECG signal was

extracted from the body surface potentials at the standardized electrode positions.

### 3. Results

#### 3.1. Eigenmodes of the bi-atrial shape model

Applying a PCA to the cut shape vectors in correspondence  $\mathbf{s}^C$  as described in Section 2.5 yields their mean shape  $\bar{\mathbf{s}}$  comprising 62,818 triangular cells and 31,745 vertices with an average edge length of 0.929 mm. Furthermore, the eigenvectors and eigenvalues of the bi-atrial model were obtained. Fig. 4 shows the shape changes caused by varying the coefficients of the first three eigenvectors. The first eigenmode represents a change in the total volume and size of both atria simultaneously (Fig. 4, first row). The second mode reflects the asymmetry of the LA vs. the RA volume, i.e., the increase of the LA volume and the concurrent decrease of the RA volume. The prominence of the right and left appendage are encoded in the third eigenmode (Fig. 4, third row). The orientation of the PVs to one another are represented – among other aspects – in the fifth, sixth, and eighth eigenmodes of the SSM.

#### 3.2. Evaluation of the bi-atrial shape model

The quality of the bi-atrial SSM was evaluated by first assessing the mean vertex to vertex distances between the meshes in correspondence and their respective original locations from the dataset. For the 47 meshes used to build the SSM, this distance was  $1.60 \pm 0.25$  mm. Furthermore, three standard evaluation criteria for evaluating the SSM quality proposed by Davies (2002) were considered: generalization, specificity, and compactness. The *generalization* metric addressed in Section 3.2.1 refers to the ability of the SSM to recreate an instance whose shape vector was excluded from the dataset used to create the SSM. The *specificity* metric (Section 3.2.2) assesses the goodness of the model in terms of generating realistic shapes. Furthermore, the *compactness* (Section 3.2.3) metric of the model increases the more the set of

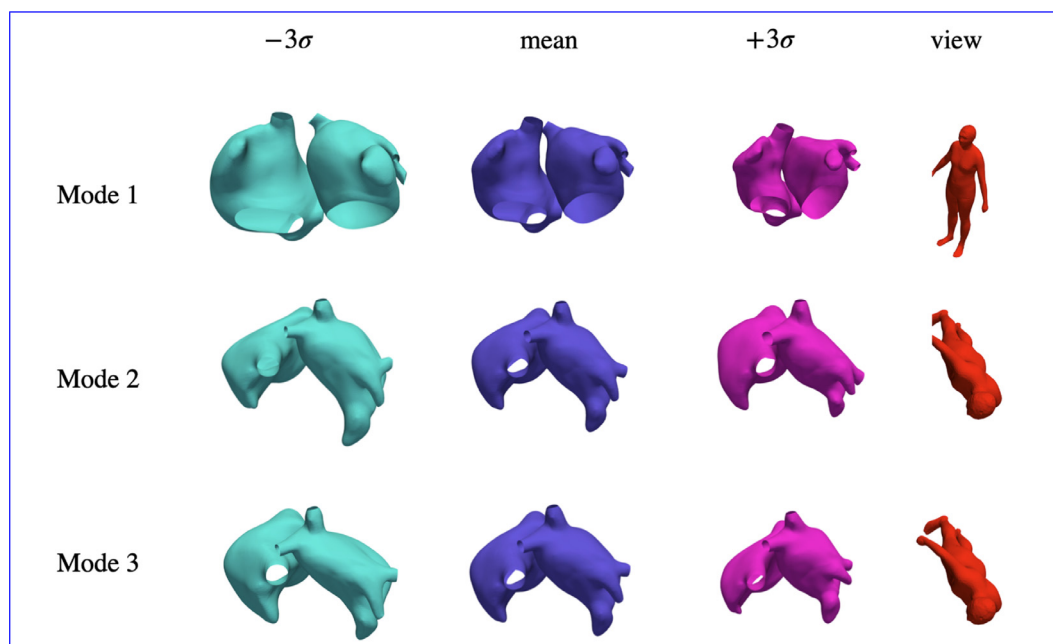


**Fig. 4.** Eigenmodes of the bi-atrial shape model. The three leading eigenmodes are displayed in different rows. Columns 1–3 represent the variation of the eigenvector coefficients. In the fourth column, the anatomical view used to capture the respective eigenmode is depicted.

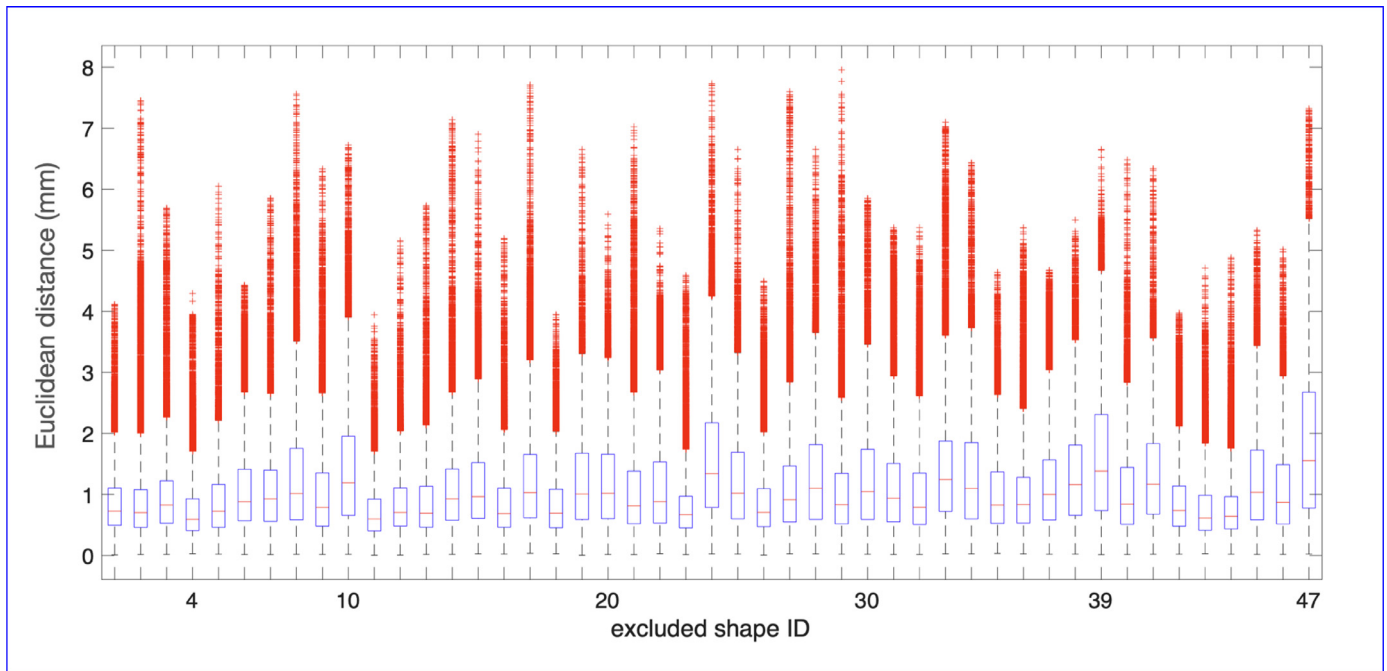


Fig. 5. Euclidean distance between vertices of the original and reconstructed shapes in mm.

eigenvectors can be reduced while still being able to describe the majority of the total shape variance present in the dataset.

### 3.2.1. Generalization

To evaluate the generalization quality of the SSM, we used leave-one-out cross-validation and defined  $N$  datasets with  $N - 1$  meshes each by leaving out the final observation. Each of those was used to compute a reduced SSM. The excluded shape was reconstructed with the reduced SSM by determining the eigenvector coefficients using ordinary least squares. The similarity between the original excluded shape and the approximated one was assessed in terms of the Euclidean distance between the corresponding vertices. Fig. 5 shows the distribution of this error metric for all instances in the dataset. The median of the vertex to vertex distance was below  $1.56\text{ mm}$  among all shapes which compares to the order of magnitude of the MRI cross-plane resolution ( $0.4\text{ mm} - 2.7\text{ mm}$ ). Instance 4, 11 and 43 hold the lowest Euclidean distances between the vertices of its original and reconstructed shape, whereas instance 47 is characterized by considerably high error values. Especially the 75th and the 95th percentile bounds comprise large vertex to vertex distances. Fig. 6 depicts the approximated atria with the reduced SSM for the instance with the highest error (47). The vertex color represents the Euclidean distance to the corresponding vertex in the original shape instance 47. Vertices showing larger deviations were located predominantly on the anterior wall and the appendages of both atria.

### 3.2.2. Specificity

The specificity of the bi-atrial model was evaluated by generating 1000 random shapes according to Eq. 2 by uniformly sampling  $\mathbf{r}$  in the interval  $[-3, 3]$ . The similarity between these random shapes and the respective closest shapes in the underlying dataset  $\mathbf{I}^C$  used to build the SSM was assessed in terms of the root mean square error (rmse) of all vertex-to-vertex distances between the randomly generated and the original shape. The rmse ranged from 4.65 to 10.83 mm among all 1000 random instances with a mean  $\pm$  standard deviation of  $7.79 \pm 1.00\text{ mm}$ . Fig. 7 shows one randomly generated shape with an rmse of 7.14 mm in yellow together with its most similar instance from the dataset in blue.

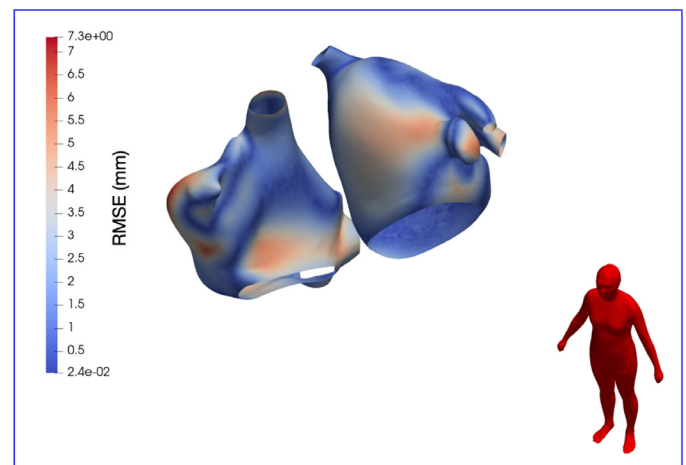


Fig. 6. Approximated shape of instance 47 with a reduced SSM built without this shape. Vertex color represents the Euclidean distance to the corresponding vertex in the original shape instance 47.

This case approximately represents the mean rmse value among all 1000 random shapes.

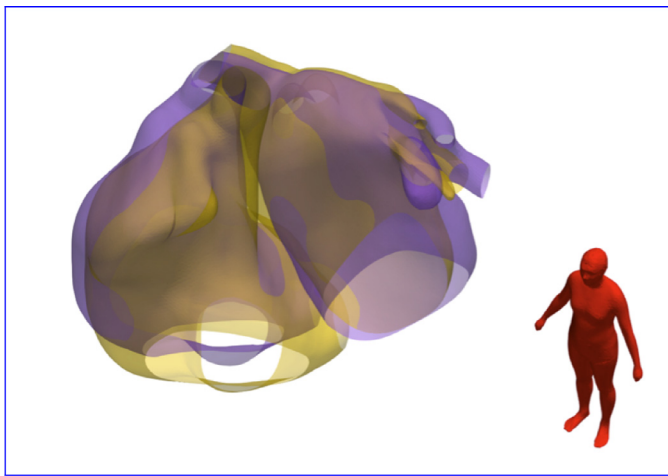
### 3.2.3. Compactness

Fig. 8 depicts the total variance of the dataset explained by the model when including only a limited number of leading eigenvectors.

90 and 95% of the total shape variance in the individual segmented shapes can be covered by the SSM when considering only the first 18 and 24 eigenvectors, respectively.

### 3.3. P wave simulations

Calculating the P wave on the mean shape of the proposed SSM as described in Section 2.7 yields the signals for the Einthoven, Goldberger and Wilson leads shown in Fig. 9. The P wave du-



**Fig. 7.** Example of one randomly generate shape with the SSM (yellow) overlaid with the closest instance in the dataset used to build the SSM (blue). (For interpretation of the references to colour in this figure legend, the reader is referred to the web version of this article.)

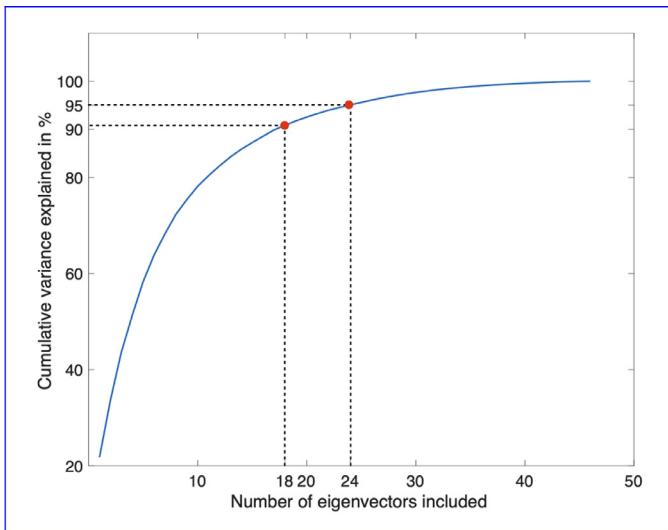


**Fig. 8.** Cumulative variance covered for different numbers of leading eigenvectors included.

ration was extracted for each of the 12-lead ECGs simulated on 100 random instances by considering the time difference between the latest detection of the P wave offset and the earliest P wave onset across all 12 leads. The values of the P wave durations - arising from simulations in which only the atrial anatomy was

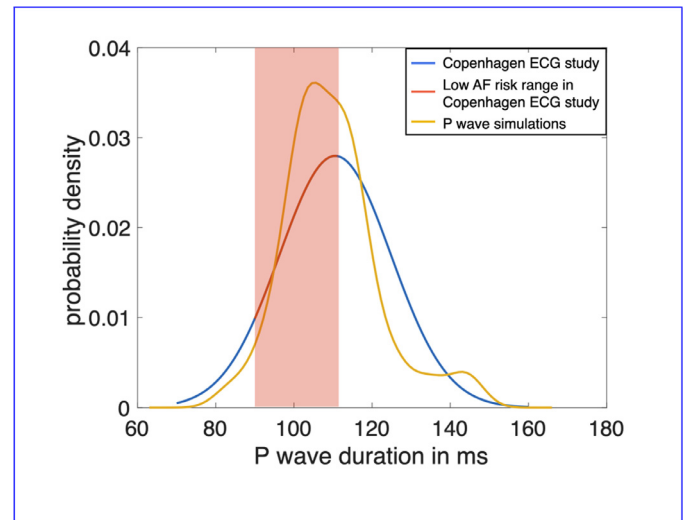


**Fig. 10.** Probability density functions of P wave durations in the Copenhagen ECG study (blue) and in our simulation study (yellow). The area highlighted in red represents the value range of patients holding a low AF risk (90–111 ms) as reported by Nielsen et al. (2015). (For interpretation of the references to colour in this figure legend, the reader is referred to the web version of this article.)

varied - ranged from 83 ms to 146 ms with a mean and standard deviation of  $109.7 \pm 12.2$  ms. The probability density of the P wave durations extracted from our simulation results are visualized in Fig. 10 in yellow. The distribution of P wave durations in the Copenhagen ECG study was reconstructed based on the values reported in Nielsen et al. (2015) and are shown in blue in Fig. 10. The interval of 90–111 ms characterizing P wave durations of subjects stratified with a low AF risk is marked in red.

### 3.4. Openly available dataset

The bi-atrial SSM is provided under the Creative Commons license CC-BY 4.0 together with 100 exemplary volumetric models derived from it including fiber orientation, inter-atrial bridges and anatomical labels (Nagel et al., 2021). Furthermore, solutions to Laplace’s equation with various boundary conditions as proposed by Piersanti et al. (2021) are provided to facilitate the derivation of universal atrial coordinates (Roney et al., 2019). The SSM is available as an h5 file encoding information about the mean shape’s spatial vertex locations and their triangulation. Also the eigenvectors and -values resulting from the applying the PCA are included. The 100 geometries were generated by sampling the eigenvector coefficients  $\mathbf{r}$  from a Gaussian distribution in the  $[-3, +3]\sigma$  range. These anatomical models are provided in VTK file format including

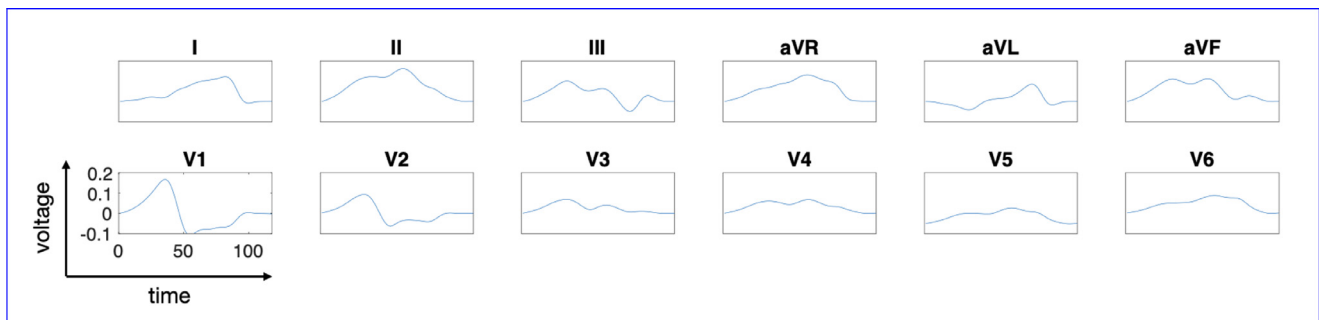


**Fig. 9.** P waves of the 12-lead ECG calculated on the mean shape of the proposed bi-atrial shape model. The red markers indicate the earliest onset and the latest offset of the P wave. (For interpretation of the references to colour in this figure legend, the reader is referred to the web version of this article.)

fiber orientation as 3D vectors and material tags as scalar values in the cell data section.

#### 4. Discussion

The main result of this study is a point distribution model incorporating the shape variations of the right and the left atrium as well as their appendages and the PVs. Moreover, we presented a workflow for building a volumetric atrial model from an endocardial surface derived from the SSM. Together with 100 example volumetric geometries generated by a Gaussian variation of the principal component coefficients in the  $[-3, +3]\sigma$  range including fiber orientation, inter-atrial bridges and anatomical labels, the SSM is openly available (Nagel et al., 2021).

Electrophysiological simulations covering atrial excitation spread and propagation of electrical potentials to the body surface were conducted on these 100 example shapes. The resulting P wave durations obtained with the proposed SSM of  $109.7 \pm 12.2$  ms are in agreement with the P wave durations of 100–105 ms reported for individuals with a very low atrial fibrillation risk in an extensive cohort study based on 285,933 ECGs (Nielsen et al., 2015). On the one hand, this suggests that our model is capable of producing a large variety of variation shapes leading to realistic ECG feature values when compared to clinical recordings. On the other hand, it implies that the additional P wave duration variability observed in individuals with increased atrial fibrillation risk (92–116 ms range covering 20–80% percentiles in Nielsen et al. (2015)) is either due to pathological anatomical variability not represented in the healthy dataset used to build this SSM or due to non-anatomical, functional changes such as conduction velocity slowing due to fibrotic infiltration of the atrial tissue (Caixal et al., 2020).

In our model, 24 eigenvectors are necessary to explain 95% of the total variance of the dataset. In the LA-only SSM built by Corrado et al. (2020), the first 15 eigenmodes cover 95% of the entire shape variance. Cates et al. (2014) reported that only 8 eigenvectors account for 95% of the total variance. However, these two models do neither consider the LAA nor the RA which explains the higher complexity of our model and in turn the need to include more eigenvectors to cover the majority of the shape variance. By allowing only a variation of the PVs' orientation in anterior-posterior direction during correspondence retrieval, we prevent changes in the PV lengths and diameters to be reflected in the model's eigenmodes, which was reported as a possible limitation of the model by Cates et al. (2014).

Varying the first eigenvector in the LA SSM published by Varela et al. (2017) causes a variation of the total LA volume as it is also the case in our model (Fig. 4). Also Corrado et al. (2020) and Cates et al. (2014) report a change of the total LA size in the first eigenmode. In the latter, the first mode represents a dilation of the LA mainly in anterior-posterior direction, which is also the case for the third eigenmode of the SSM built by Corrado et al. (2020), where the first eigenmode rather represents an elongation of the LA in medial-lateral direction. Cates et al. (2014) also constructed a separate SSM of the LAA and found that its first shape parameter corresponds to a change in the LAA length which is as well described by the third eigenmode of our model.

The shape variations encoded in the leading eigenmodes of our novel bi-atrial SSM are consistent with previously published LA-only SSMs as far as the LA is concerned. This demonstrates that our model is able to reflect the same main shape variations even though it is based on a dataset of less than half the size compared to the other models. The second eigenmode of our model represents the asymmetry between right and left atrial volume. This further manifests the novel insights into inter-subject atrial geometry

variations revealing with our model since this shape change cannot be captured with two separate RA and LA SSMs.

The generalization results demonstrate that our model is able to accurately predict the shape of a previously unseen atrial geometry. The specificity results of  $7.79 \pm 1.00$  mm leave room for improvement. However, the low specificity scores do not result from unanatomical characteristics of the generated shapes. They occur rather due to the small dataset of 47 instances available for selecting the closest shape during evaluation. Considering the MR slice thickness of predominantly 2.7 mm (Table 1), a specificity rmse of 7.79 mm is in the range of less than 2 voxel diameters with segmentation uncertainty adding to it (Karim et al., 2018). The specificity evaluation of our model therefore indicates that randomly generated shapes produce valid shapes with an accuracy in the range of the error susceptibility during segmentation.

The atria segmented for this study originate from datasets comprising images of not only healthy subjects but also patients with a known history of atrial fibrillation. LA enlargement has been linked with an increased risk for this arrhythmia (Andlauer et al., 2018; Broughton et al., 2016; Hamatani et al., 2016). To ensure that our model is not based on a biased dataset with predominantly enlarged left atria, the LA volume (excluding LAA and PV ostia) of the  $N$  segmented geometries ( $82.16 \pm 19.16$  ml) was compared to reference values. Pritchett et al. (2003) considered all age and BMI groups in healthy individuals. Translating their 2D measurements to 3D volumes as suggested by Al-Mohaisen et al. (2013) yields a  $[-3, +3]\sigma$  range of 10–130 ml with the largest LA volume in our dataset (122 ml) being within that range. In this way, we were able to keep the dataset as large as possible. For the same reason, we also did not exclude any geometries segmented from different image modalities or different spatial resolutions, which might however impact the shape statistics of the SSM. The largest slice thickness (2.7 mm) is in the range recommended in Salerno et al. (2017) and relied on in previous studies (Cates et al., 2014; Corrado et al., 2020). This indicates that the coarsest spatial resolution in our training dataset was still sufficient to allow covering all relevant anatomical structures during segmentation. Regarding segmentation, we relied as much as possible on the ground truth LA shapes provided publicly available along with the datasets and the automated segmentation workflows in CemrgApp. However, since manual corrections were indispensable in some cases (see Fig. 1), inter- and intra-observer variabilities might still have had an impact on the final segmentation outcome.

Due to the highly complex shape and the natural clustering of the LAA, we categorized the shape of this structure for all 47 subjects into four classes as proposed by Wang et al. (2010). 11%, 47%, 36% and 6% of our segmented shapes were assigned to the ChickenWing, WindSock, Cauliflower and Cactus morphology classes, respectively. Examples from our dataset assigned to each of the four shape clusters are shown in Fig. 11. The distribution of the LAA shape in the four categories are in accordance with the frequency of occurrence of the 612 LAA shapes studied by Wang et al. (2010) in each class. This demonstrates that our dataset also exhibits similar variability concerning the LAA shape as observed in larger cohort studies.

We chose the PCA representation to describe the atrial shape variability and thereby assumed the changes in the atrial shape to be Gaussian distributed which does not hold true for the entire inter-patient shape variability (Bieging et al., 2018; Wang et al., 2010). For the sake of comparability with previously published models and for reproducibility, we intentionally decided for this state-of-the-art approach. Furthermore, the reference shape for the rigid alignment and the correspondence retrieval was chosen to be the geometry with the smallest mean vertex to nearest neighbor distance to the other shapes. The choice of the reference mesh for ICP only influences the alignment results regarding the final ori-

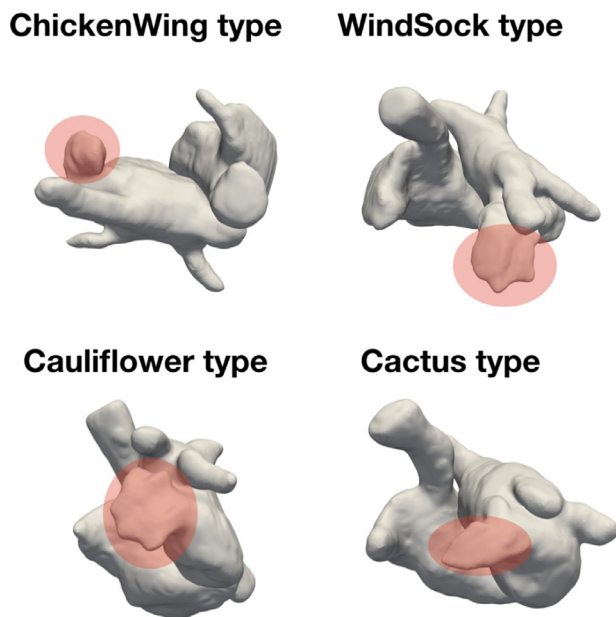


**Fig. 11.** Examples from our dataset assigned to the different LAA shape clusters as proposed by Wang et al. (2010). The ChickenWing type differs from the other types by a sharp bend, the WindSock type is characterized by secondary lobes only in inferior direction, the Cactus type in inferior and superior direction. The Cauliflower type doesn't exhibit any clear primary lobe.

entation of all aligned meshes. Since the mean vertex-to-vertex distances between the meshes in correspondence and the original instances quantified to  $1.60 \pm 0.25$  mm, it can be inferred that the fitting algorithm for correspondence retrieval performed sufficiently well. Therefore, the choice of the reference shape should not have any major influence on the correspondence estimate. In contrast, with the particular choice of our reference mesh, we facilitate that the deformed atlas is still capable of representing finer structural changes present in other models and prevent that finer structures that would only be present in the atlas are over-represented in the final SSM.

To showcase a potential application, we conducted multi-scale electrophysiological simulations on 100 instances of the shape model. This proof of concept was deliberately based on a simple model not considering locally heterogeneous atrial wall thickness (Azzolin et al., 2020; Karim et al., 2018; Whitaker et al., 2016), disease-induced remodeling of membrane dynamics (Loewe et al., 2014) or diffusive aspects during cardiac depolarization. Also only one torso shape and no rotation and translation of the atria within the torso are considered. The pipeline to generate volumetric models and simulation setups from the SSM is prepared for such extensions, though. Even though the shape variability covered by our model only comprises anatomical variants that were present in the dataset, i.e. healthy and AF patients without considerably enlarged left atrial volumes, the geometries can still be used for simulations of pathologies not affecting the atrial anatomy but reflecting in non-healthy functional anomalies, for example conduction blocks or ionic remodeling processes. Future studies focusing on repolarization could replace the simplistic Eikonal coupling employed here with a reaction-Eikonal scheme as suggested by Neic et al. (2017).

The main advantage of the novel bi-atrial SSM consists in the automated generation of a large number of atrial geometries. In this way, the cumbersome and time-consuming process of anatomical model generation involving MRI segmentation and defining bundles and fiber orientation can be facilitated and expedited.

Potse et al. (2018) examined the influence of electrical and structural remodeling on the maintenance of complex reentrant activity. With our proposed bi-atrial SSM, also the influence of the general atrial anatomy on the perpetuation and initialization of atrial fibrillation can be quantified.

Saha et al. (2016) investigated the effect of endo-epicardial activation delay on the P wave morphology. However, only one atrial geometry was used to deduce models of different atrial wall thicknesses in this study and the authors state the lack of using different geometries as a limitation of their work. The same limitation is listed in the study of Pezzuto et al. (2018) aiming at quantifying the beat-to-beat variability of P waves in patients with atrial fibrillation. With our SSM, a larger number of different volumetric atrial models is easily acquirable.

By means of our bi-atrial SSM, scale-large cohort studies using computer models for simulating atrial activity become feasible. Luongo et al. (2020b,a) found a significant influence of the number of atrial anatomies included on the classification of different types of atrial flutter with a machine learning approach. With the proposed SSM, a large number of geometries can be deduced and used as a basis for in silico big data approaches such as to produce extensive datasets for machine learning applications. The provided instances are ready to be used off the shelf in available computational simulation environments such as openCARP for electrophysiology (Sánchez et al., 2020), openFOAM for fluid dynamics (Jasak, 2009) or FEniCS for continuum-mechanics (Alnæs et al., 2015).

## 5. Conclusions

To the best of our knowledge, we built the first SSM incorporating both atria, their appendages and the orientation of the PVs. The model itself and 100 random volumetric atrial geometries including rule-based fiber orientation and anatomical labelling were made publicly available to the community which we consider as the main added value of our study. These models are ready to be used off-the-shelf for electrophysiological simulations. Established quality criteria indicate that the novel SSM can be reduced to a set of 24 eigenvectors and is capable of generalizing well to unseen geometries. P waves simulated on 100 random instances derived from the SSM reproduce the P wave distribution observed in clinical ECGs of healthy individuals. As such, the SSM is suitable to generate comprehensive model cohorts covering the relevant anatomical variability as a basis for large-scale in silico simulations including, but not limited to, ECG simulations for machine learning applications.

## Declaration of Competing Interest

The authors declare that they have no known competing financial interests or personal relationships that could have appeared to influence the work reported in this paper.

## CRediT authorship contribution statement

**Claudia Nagel:** Conceptualization, Methodology, Software, Investigation, Validation, Formal analysis, Writing – original draft, Visualization, Data curation. **Steffen Schuler:** Conceptualization, Methodology, Software. **Olaf Dössel:** Writing – review & editing, Supervision, Project administration, Funding acquisition, Resources. **Axel Loewe:** Conceptualization, Methodology, Writing – review & editing, Supervision, Project administration, Funding acquisition, Resources.

## Acknowledgments

This work was supported by the EMPIR programme co-financed by the participating states and from the European Union's Horizon 2020 research and innovation programme under grant MedalCare 18HLT07. We would like to thank the reviewers for their valuable comments contributing to the improvement of our work.

## References

- Aguado, A.M., Olivares, A.L., Yagüe, C., Silva, E., Nuñez-García, M., Fernandez-Quilez, A., Mill, J., Genua, I., Arzamendi, D., De Potter, T., Freixa, X., Camara, O., 2019. In silico optimization of left atrial appendage occluder implantation using interactive and modeling tools. *Front Physiol* 10. doi:10.3389/fphys.2019.00237.
- Al-Mohaisen, M.A., Kazmi, M.H., Chan, K.L., Chow, B.J.W., 2013. Validation of two-dimensional methods for left atrial volume measurement: a comparison of echocardiography with cardiac computed tomography. *Echocardiography* 30 (10), 1135–1142. doi:10.1111/echo.12253.
- Alnæs, M.S., Blechta, J., Hake, J., Johansson, A., Kehlet, B., Logg, A., Richardson, C., Ring, J., Rognes, M.E., Wells, G.N., 2015. The fenics project version 1.5. *Archive of Numerical Software* 3 (100). doi:10.11588/ans.2015.100.20553.
- Andlauer, R., Seemann, G., Baron, L., Dössel, O., Kohl, P., Platonov, P., Loewe, A., 2018. Influence of left atrial size on p-wave morphology: differential effects of dilation and hypertrophy. *Europace* 20 (S3), iii36–iii44. doi:10.1093/europace/euy231.
- Azzolin, L., Luongo, G., Rocher, S., Saiz, J., Doessel, O., Loewe, A., 2020. Influence of gradient and smoothness of atrial wall thickness on initiation and maintenance of atrial fibrillation. In: *Computing in Cardiology Conference (CinC)*.
- Bai, W., Shi, W., de Marvao, A., Dawes, T.J., O'Regan, D.P., Cook, S.A., Rueckert, D., 2015. A bi-ventricular cardiac atlas built from 1000+ high resolution MR images of healthy subjects and an analysis of shape and motion. *Med Image Anal* 26 (1), 133–145. doi:10.1016/j.media.2015.08.009.
- Bieging, E.T., Morris, A., Wilson, B.D., McGann, C.J., Marrouche, N.F., Cates, J., 2018. Left atrial shape predicts recurrence after atrial fibrillation catheter ablation. *J. Cardiovasc. Electrophysiol* 29 (7), 966–972. doi:10.1111/jce.13641.
- Bouabene, G., Gerig, T., Luethi, M., Forster, A., Madsen, D., Rahbani, D., Kahr, P., 2020. Scalismolab: Scalable Image Analysis and Shape Modelling. Accessed December 2, 2020.
- Broughton, S.T., O'Neal, W.T., Salahuddin, T., Soliman, E.Z., 2016. The influence of left atrial enlargement on the relationship between atrial fibrillation and stroke. *J Stroke Cerebrovasc Dis* 25 (6), 1396–1402. doi:10.1016/j.jstrokecerebrovasdis.2016.02.004.
- Caixal, G., Alarcón, F., Althoff, T.F., Nuñez-García, M., Benito, E.M., Borrás, R., Perea, R.J., Prat-González, S., Garre, P., Soto-Iglesias, D., Gunturitz, C., Cozzari, J., Linhart, M., Tolosana, J.M., Arbelo, E., Roca-Luque, I., Sitges, M., Guasch, E., Mont, L., 2020. Accuracy of left atrial fibrosis detection with cardiac magnetic resonance: correlation of late gadolinium enhancement with endocardial voltage and conduction velocity. *Europace* doi:10.1093/europace/eaab313.
- Cates, J., Bieging, E., Morris, A., Gardner, G., Akoum, N., Kholmovski, E., Marrouche, N., McGann, C., MacLeod, R.S., 2014. Computational shape models characterize shape change of the left atrium in atrial fibrillation. *Clin Med Insights Cardiol* 8 (Suppl 1), 99–109. doi:10.4137/CMC.S15710.
- Chen, Y., Medioni, G., 1992. Object modelling by registration of multiple range images. *Image Vis Comput* 10 (3), 145–155. doi:10.1016/0262-8856(92)90066-C.
- Cootes, T.F., Taylor, C.J., Cooper, D.H., Graham, J., 1995. Active shape models - their training and application. *Comput. Vision Image Understanding* 61 (1), 38–59.
- Corrado, C., Razeghi, O., Roney, C., Coveney, S., Williams, S., Sim, I., O'Neill, M., Wilkinson, R., Oakley, J., Clayton, R.H., Niederer, S., 2020. Quantifying atrial anatomy uncertainty from clinical data and its impact on electro-physiology simulation predictions. *Med Image Anal* 61, 101626. doi:10.1016/j.media.2019.101626.
- Courtemanche, M., Ramirez, R.J., Nattel, S., 1998. Ionic mechanisms underlying human atrial action potential properties: insights from a mathematical model. *Am. J. Physiol.* 275 (1), H301–21. doi:10.1152/ajpheart.1998.275.1.H301.
- Davies, R., 2002. Learning shape: optimal models for analysing natural variability. Depa, M., Sabuncu, M.R., Holmvang, G., Nezafat, R., Schmidt, E.J., Golland, P., 2010. Robust atlas-based segmentation of highly variable anatomy: left atrium segmentation. *Statistical atlases and computational models of the heart. STACOM (Workshop)* 6364, 85–94. doi:10.1007/978-3-642-15835-3\_9.
- Ecabert, O., Peters, J., Schramm, H., Lorenz, C., von Berg, J., Walker, M.J., Vembar, M., Olszewski, M.E., Subramanyan, K., Lavi, G., Weese, J., 2008. Automatic model-based segmentation of the heart in CT images. *IEEE Trans Med Imaging* 27 (9), 1189–1201. doi:10.1109/TMI.2008.918330.
- Geuzaine, C., Remacle, J.-F., 2009. Gmsh: a 3-d finite element mesh generator with built-in pre- and post-processing facilities. *Int J Numer Methods Eng* 79 (11), 1309–1331. doi:10.1002/nme.2579.
- Hamatani, Y., Ogawa, H., Takabayashi, K., Yamashita, Y., Takagi, D., Esato, M., Chun, Y.-H., Tsuji, H., Wada, H., Hasegawa, K., Abe, M., Lip, G.Y.H., Akao, M., 2016. Left atrial enlargement is an independent predictor of stroke and systemic embolism in patients with non-valvular atrial fibrillation. *Sci Rep* 6, 31042. doi:10.1038/srep31042.
- Hannun, A.Y., Rajpurkar, P., Haghpanahi, M., Tison, G.H., Bourn, C., Turakhia, M.P., Ng, A.Y., 2019. Cardiologist-level arrhythmia detection and classification in ambulatory electrocardiograms using a deep neural network. *Nat. Med.* 25 (1), 65–69. doi:10.1038/s41591-018-0268-3.
- Hoogendoorn, C., Duchateau, N., Sánchez-Quintana, D., Whitmarsh, T., Sukno, F.M., De Craene, M., Lekadir, K., Frangi, A.F., 2013. A high-resolution atlas and statistical model of the human heart from multislice CT. *IEEE Trans Med Imaging* 32 (1), 28–44. doi:10.1109/TMI.2012.2230015.
- Jakob, W., Tarini, M., Panozzo, D., Sorkine-Hornung, O., 2015. Instant field-aligned meshes. *ACM Trans Graph* 34 (6), 1–15. doi:10.1145/2816795.2818078.
- Jasak, H., 2009. OpenFOAM: open source CFD in research and industry. *International Journal of Naval Architecture and Ocean Engineering* 1, 89–94. doi:10.2478/jinaoe-2013-0011.
- Kahlmann, W., Poremba, E., Potyagaylo, D., Dössel, O., Loewe, A., 2017. Modelling of patient-specific purkinje activation based on measured ECGs. In: *Current Directions in Biomedical Engineering*. de Gruyter, pp. 171–174. doi:10.1515/cdbme-2017-0177.
- Karim, R., Blake, L.-E., Inoue, J., Tao, Q., Jia, S., Housden, R.J., Bhagirath, P., Duval, J.-L., Varela, M., Behar, J., Cadour, L., van der Geest, R.J., Cochet, H., Drangova, M., Serresant, M., Razavi, R., Aslanidi, O., Rajani, R., Rhode, K., 2018. Algorithms for left atrial wall segmentation and thickness - evaluation on an open-source CT and MRI image database. *Med Image Anal* 50, 36–53. doi:10.1016/j.media.2018.08.004.
- Karim, R., Housden, R.J., Balasubramaniam, M., Chen, Z., Perry, D., Uddin, A., Al-Beyatti, Y., Palkhi, E., Acheampong, P., Obom, S., Hennemuth, A., Lu, Y., Bai, W., Shi, W., Gao, Y., Peitgen, H.-O., Radau, P., Razavi, R., Tannenbaum, A., Rueckert, D., Cates, J., Schaeffter, T., Peters, D., MacLeod, R., Rhode, K., 2013. Evaluation of current algorithms for segmentation of scar tissue from late gadolinium enhancement cardiovascular magnetic resonance of the left atrium: an open-access grand challenge. *J Cardiovasc Magn Reson* 15, 105. doi:10.1186/1532-429X-15-105.
- Loewe, A., Krueger, M.W., Holmqvist, F., Dössel, O., Seemann, G., Platonov, P.G., 2016. Influence of the earliest right atrial activation site and its proximity to inter-atrial connections on p-wave morphology. *Europace* 18 (suppl 4), iv35–iv43. doi:10.1093/europace/euw349.
- Loewe, A., Poremba, E., Oesterlein, T., Luik, A., Schmitt, C., Seemann, G., Dössel, O., 2019. Patient-specific identification of atrial flutter vulnerability: a computational approach to reveal latent reentry pathways. *Front Physiol* 9. doi:10.3389/fphys.2018.01910.
- Loewe, A., Wilhelms, M., Dössel, O., Seemann, G., 2014. Influence of chronic atrial fibrillation induced remodeling in a computational electrophysiological model. In: *Biomedizinische Technik / Biomedical Engineering*. Walter de Gruyter, Berlin, Boston, pp. S929–S932. doi:10.1515/bmt-2014-5012.
- Luongo, G., Schuler, S., Luik, A., Almeida, T.P., Soriano, D.C., Doessel, O., Loewe, A., 2020. Non-invasive characterization of atrial flutter mechanisms using recurrence quantification analysis on the ECG: a computational study. *IEEE Trans Biomed Eng* doi:10.1109/TBME.2020.2990655.
- Luongo, G., Schuler, S., Rivolta, M.W., Dössel, O., Sassi, R., Loewe, A., 2020. Automatic ECG-based discrimination of 20 atrial flutter mechanisms: Influence of atrial and torso geometries. In: *Computing in Cardiology Conference (CinC)*.
- Luthi, M., Gerig, T., Jud, C., Vetter, T., 2018. Gaussian process morphable models. *IEEE Trans Pattern Anal Mach Intell* 40 (8), 1860–1873. doi:10.1109/TPAMI.2017.2739743.
- Lötjönen, J., Kivistö, S., Koikkalainen, J., Smutek, D., Lauerma, K., 2004. Statistical shape model of atria, ventricles and epicardium from short- and long-axis MR images. *Med Image Anal* 8 (3), 371–386. doi:10.1016/j.media.2004.06.013.
- Marom, E.M., Herndon, J.E., Kim, Y.H., McAdams, H.P., 2004. Variations in pulmonary venous drainage to the left atrium: implications for radiofrequency ablation. *Radiology* 230 (3), 824–829. doi:10.1148/radiol.2303030315.
- Masci, A., Barone, L., Dedé, L., Fedele, M., Tomasi, C., Quarteroni, A., Corsi, C., 2019. The impact of left atrium appendage morphology on stroke risk assessment in atrial fibrillation: a computational fluid dynamics study. *Front Physiol* 9. doi:10.3389/fphys.2018.01938.
- Nagel, C., Sanchez, J., Azzolin, L., Zheng, T., Schuler, S., Dössel, O., Loewe, A., 2021. A Bi-atrial Statistical Shape Model and 100 Volumetric Anatomical Models of the Atria. doi:10.5281/zenodo.5004620.
- Neic, A., Campos, F.O., Prassl, A.J., Niederer, S.A., Bishop, M.J., Vigmond, E.J., Plank, G., 2017. Efficient computation of electrograms and ECGs in human whole heart simulations using a reaction-eikonal model. *J Comput Phys* 346, 191–211. doi:10.1016/j.jcp.2017.06.020.
- Nielsen, J.B., Kuhl, J.T., Pietersen, A., Graff, C., Lind, B., Struijk, J.J., Olesen, M.S., Sinner, M.F., Bachmann, T.N., Haunso, S., Nordestgaard, B.G., Ellinor, P.T., Svendsen, J.H., Kofoed, K.F., Kober, L., Holst, A.G., 2015. P-Wave duration and the risk of atrial fibrillation: results from the copenhagen ECG study. *Heart Rhythm* 12 (9), 1887–1895. doi:10.1016/j.hrthm.2015.04.026.
- Nishimura, M., Lupercio-Lopez, F., Hsu, J.C., 2019. Left atrial appendage electrical isolation as a target in atrial fibrillation. *JACC Clin Electrophysiol* 5 (4), 407–416. doi:10.1016/j.jacep.2019.02.009.
- Ordas, S., Oubel, E., Sebastian, R., Frangi, A. F., 2007. Computational anatomy atlas of the heart. 338–342. doi:10.1109/ISPA.2007.4383715.
- Perez Alday, E. A., Gu, A., Shah, A., Robichaux, C., Wong, A.-K. I., Liu, C., Liu, F., Rad, A. B., Elola, A., Seyed, S., Li, Q., Sharma, A., Clifford, G. D., Reyna, M. A., 2020. Classification of 12-lead ECGs: the physionet/computing in cardiology challenge 2020. doi:10.1101/2020.08.11.20172601.
- Pezzuto, S., Gharaviri, A., Schotten, U., Potse, M., Conte, G., Caputo, M.L., Regoli, F., Krause, R., Auricchio, A., 2018. Beat-to-beat p-wave morphological variability in patients with paroxysmal atrial fibrillation: an in silico study. *Europace* 20, iii26–iii35. doi:10.1093/europace/euy227. suppl\_3
- Piersanti, R., Africa, P.C., Fedele, M., Vergara, C., Dedé, L., Corno, A.F., Quarteroni, A., 2021. Modeling cardiac muscle fibers in ventricular and atrial electrophysiology

- simulations. *Comput Methods Appl Mech Eng* 373, 113468. doi:[10.1016/j.cma.2020.113468](https://doi.org/10.1016/j.cma.2020.113468).
- Pishchulin, L., Wuhrer, S., Helten, T., Theobalt, C., Schiele, B., 2017. Building statistical shape spaces for 3d human modeling. *Pattern Recognit* 67, 276–286. doi:[10.1016/j.patcog.2017.02.018](https://doi.org/10.1016/j.patcog.2017.02.018).
- Potse, M., Gharaviri, A., Pezzuto, S., Auricchio, A., Krause, R., Verheule, S., Schotten, U., 2018. Anatomically-induced fibrillation in a 3d model of the human atria 45. doi:[10.22489/CinC.2018.366](https://doi.org/10.22489/CinC.2018.366).
- Pritchett, A.M., Jacobsen, S.J., Mahoney, D.W., Rodeheffer, R.J., Bailey, K.R., Redfield, M.M., 2003. Left atrial volume as an index of left atrial size: a population-based study. *J. Am. Coll. Cardiol* 41 (6), 1036–1043. doi:[10.1016/S0735-1097\(02\)02981-9](https://doi.org/10.1016/S0735-1097(02)02981-9).
- Razeghi, O., Solís-Lemus, J.A., Lee, A.W., Karim, R., Corrado, C., Roney, C.H., de Vecchi, A., Niederer, S.A., 2020. Cemrgapp: an interactive medical imaging application with image processing, computer vision, and machine learning toolkits for cardiovascular research. *SoftwareX* 12, 100570. doi:[10.1016/j.softx.2020.100570](https://doi.org/10.1016/j.softx.2020.100570).
- Roney, C.H., Pashaie, A., Meo, M., Dubois, R., Boyle, P.M., Trayanova, N.A., Cochet, H., Niederer, S.A., Vigmond, E.J., 2019. Universal atrial coordinates applied to visualisation, registration and construction of patient specific meshes. *Med Image Anal* 55, 65–75. doi:[10.1016/j.media.2019.04.004](https://doi.org/10.1016/j.media.2019.04.004).
- Saha, M., Conte, G., Caputo, M.L., Regoli, F., Krause, R., Auricchio, A., Jacquemet, V., 2016. Changes in p-wave morphology after pulmonary vein isolation: insights from computer simulations. *Europace* 18 (suppl 4), iv23–iv34. doi:[10.1093/europace/euw348](https://doi.org/10.1093/europace/euw348).
- Salerno, M., Sharif, B., Arheden, H., Kumar, A., Axel, L., Li, D., Neubauer, S., 2017. Recent advances in cardiovascular magnetic resonance: techniques and applications. *Circ Cardiovasc Imaging* 10 (6). doi:[10.1161/CIRCIMAGING.116.003951](https://doi.org/10.1161/CIRCIMAGING.116.003951).
- Schuler, S., Tate, J.D., Oostendorp, T.F., MacLeod, R.S., Dössel, O., 2019. Spatial down-sampling of surface sources in the forward problem of electrocardiography. In: Coudière, Y., Ozanne, V., Vigmond, E., Zemzemi, N. (Eds.), *Functional Imaging and Modeling of the Heart*. Springer International Publishing, pp. 29–36. doi:[10.1007/978-3-030-21949-9\\_4](https://doi.org/10.1007/978-3-030-21949-9_4).
- Sethian, J.A., 1996. A fast marching level set method for monotonically advancing fronts. *Proc. Natl. Acad. Sci. U.S.A.* 93 (4), 1591–1595.
- Stenroos, M., Mäntynen, V., Nenonen, J., 2007. A matlab library for solving quasi-static volume conduction problems using the boundary element method. *Comput Methods Programs Biomed* 88 (3), 256–263.
- Strothoff, N., Wagner, P., Schaeffter, T., Samek, W., 2020. Deep learning for ECG analysis: Benchmarks and insights from PTB-XL.
- Sánchez, J., Nothstein, M., Neic, A., Huang, Y.-L., Prassl, A.J., Klar, J., Ulrich, R., Bach, F., Zschumme, P., Selzer, M., Plank, G., Vigmond, E., Seemann, G., Loewe, A., 2020. openCARP: An open sustainable framework for in-silico cardiac electrophysiology research. In: *Computing in Cardiology Conference (CinC)*, 47.
- Tobon-Gomez, C., Geers, A.J., Peters, J., Weese, J., Pinto, K., Karim, R., Ammar, M., Daoudi, A., Margeta, J., Sandoval, Z., Stender, B., Yefeng, Z., Zuluaga, M.A., Betancur, J., Ayache, N., Amine Chikh, M., Dillenseger, J.-L., Kelm, B.M., Mahmoudi, S., Ourselin, S., Schlaefter, A., Schaeffter, T., Razavi, R., Rhode, K.S., 2015. Benchmark for algorithms segmenting the left atrium from 3d CT and MRI datasets. *IEEE Trans Med Imaging* 34 (7), 1460–1473. doi:[10.1109/TMI.2015.2398818](https://doi.org/10.1109/TMI.2015.2398818).
- Tran, A.P., Yan, S., Fang, Q., 2020. Improving model-based functional near-infrared spectroscopy analysis using mesh-based anatomical and light-transport models. *Neurophotonics* 7 (1), 015008. doi:[10.1117/1.NPh.7.1.015008](https://doi.org/10.1117/1.NPh.7.1.015008).
- Unberath, M., Maier, A., Fleischmann, D., Hornegger, J., Fahrigr, R., 2015. Open-source 4d statistical shape model of the heart for x-ray projection imaging. 739–742. doi:[10.1109/ISBI.2015.7163978](https://doi.org/10.1109/ISBI.2015.7163978).
- Varela, M., Bisbal, F., Zacur, E., Berruero, A., Aslanidi, O.V., Mont, L., Lamata, P., 2017. Novel computational analysis of left atrial anatomy improves prediction of atrial fibrillation recurrence after ablation. *Front Physiol* 8, 68. doi:[10.3389/fphys.2017.00068](https://doi.org/10.3389/fphys.2017.00068).
- Wachter, A., Loewe, A., Krueger, M.W., Dössel, O., Seemann, G., 2015. Mesh structure-independent modeling of patient-specific atrial fiber orientation. *De Gruyter*, pp. 409–412. doi:[10.1515/cdbme-2015-0099](https://doi.org/10.1515/cdbme-2015-0099).
- Wang, Y., Di Biase, L., Horton, R.P., Nguyen, T., Morhanty, P., Natale, A., 2010. Left atrial appendage studied by computed tomography to help planning for appendage closure device placement. *J. Cardiovasc. Electrophysiol* 21 (9), 973–982. doi:[10.1111/j.1540-8167.2010.01814.x](https://doi.org/10.1111/j.1540-8167.2010.01814.x).
- Whitaker, J., Rajani, R., Chubb, H., Gabrawi, M., Varela, M., Wright, M., Niederer, S., O'Neill, M.D., 2016. The role of myocardial wall thickness in atrial arrhythmogenesis. *Europace* 18 (12), 1758–1772. doi:[10.1093/europace/euw014](https://doi.org/10.1093/europace/euw014).
- Zhuang, X., Rhode, K.S., Razavi, R.S., Hawkes, D.J., Ourselin, S., 2010. A registration-based propagation framework for automatic whole heart segmentation of cardiac MRI. *IEEE Trans Med Imaging* 29 (9), 1612–1625. doi:[10.1109/TMI.2010.2047112](https://doi.org/10.1109/TMI.2010.2047112).